Chinese Journal of Structural Chemistry

ARTICLE

Synergism of 1D CdS/2D Modified $Ti_3C_2T_x$ MXene Heterojunctions for Boosted Photocatalytic Hydrogen Production

Shi Cheng[1], Qianqian Xiong[1], Chengxiao Zhao[1]* and Xiaofei Yang[1]*

[1]*College of Science, Nanjing Forestry University, Nanjing 210037, China*

ABSTRACT Rational design and controllable synthesis of visible-light-responsive photocatalysts that exhibit both good hydrogen-producing efficiency and stability in the water splitting reaction are undoubtedly a challenge. Here we report an integrated CdS nanorod/oxygen-terminated $Ti_3C_2T_x$ MXene nanosheet heterojunction with a high catalytic hydrogen evolution reaction (HER) activity. By incorporating one-dimensional (1D) CdS nanorods onto annealed ultrathin two-dimensional (2D) MXene nanosheets, the mixed-dimensional 1D/2D heterojunction achieved a hydrogen-evolving rate of 8.87 $mmol \cdot g^{-1} \cdot h^{-1}$, much higher than that of bulk CdS and CdS/unmodified MXene hybrid catalysts. The enhanced HER activity and stability of the designed heterojunction catalyst are attributed to the presence of oxygen-containing terminal groups on the surface of thermally treated $Ti_3C_2T_x$ MXene, extended light absorption spectra as well as the precisely constructed intimate Schottky contact, implying an accelerated interfacial charge transfer and efficient, long-term photocatalytic hydrogen production performance. The results demonstrate that oxygen-terminated 2D MXene can be well utilized as a functional platform for the development of novel heterojunction photocatalysts.

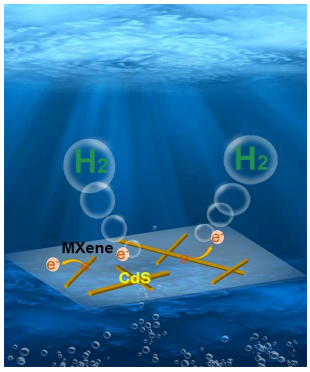

Keywords: CdS, MXene, heterojunction, water splitting, hydrogen evolution reaction

INTRODUCTION

With the continuous development of economy, the energy crisis is becoming more and more serious. Solar energy is the most abundant and clean energy, and converting solar energy into chemical fuels is highly desirable. Photocatalytic hydrogen production from water splitting driven by solar energy has been considered as a promising solution to global energy crisis.[1-8] Over the past few decades, semiconductor-based photocatalysis technology has been widely employed in the applications of CO_2 reduction, water splitting, N_2 fixation and environmental remediation.[9-17] The semiconductors, such as CdS, TiO_2, ZnS, WO_3, Fe_2O_3, Bi_2S_3, etc., are able to act as photoactive materials for redox/change-transfer processes.[18-25] Among them, highly efficient photocatalytic hydrogen production over cadmium sulfide (CdS) is well documented, originating from its good visible light-harvesting property and the matched band structure.[26-33] However, its deficiencies including rapid electron-hole recombination rate, serious photocorrosion and insufficient active sites impede the practical application in energy and environmental science.[26-31,34] Thus, rationally designing CdS-based catalysts with high hydrogen-evolving activity and enhanced stability via accelerating the separation of charge carries and facilitating interfacial charge transport is of great importance.

Integrating CdS with different co-catalysts to construct various heterojunctions has proven to be effective in enhancing hydrogen evolution reaction activity and long-term stability.[10,11,30,35,36] MXene, which is a newly discovered two-dimensional (2D) transition metal nitride/carbide, has emerged as a multifunctional material with excellent performance, showing great prospects for catalysis-related applications.[35,37-39] MXene has the general composition of $M_{n+1}X_nT_x$, where M is an early transition metal, X can be carbon or nitrogen, n = 1, 2, 3, and T_x represents surface functional groups (-O, -OH and -F).[40,41] It possesses multiple advantages of ultrathin 2D layered structure, high percentage of exposed metal atoms, regulable surface terminations, highly hydrophilic surface, wide-spectrum light absorption, and excellent electrical conductivity, providing a universal platform for constructing solar-driven heterojunction photocatalysts.[42-44]

The size and thickness of 2D MXene play an important role in determining the electrical conductivity, interfacial charge transfer and the hydrogen-producing activity. Moreover, the surface terminations of 2D MXene are highly dependent on a number of factors including the etching method, delamination process and exfoliation solvent.[44-47] Generally, ultrathin MXene nanosheets can be synthesized via the combination of top-down wet chemical etching and controllable delamination, which intrinsically results in the coexistence of different terminal groups including hydroxyl, oxygen and fluoride (-OH, -O and -F) on the surface of MXene.[48] It is well-known that oxygen-containing terminal groups majorly affect the band structure and electrical conductivity of MXene, and subsequently make a great impact on the co-catalyst-assisted photocatalytic hydrogen evolution reaction.[40,49-52]

In this paper, a thermal treatment strategy has been applied to regulate the oxygen-terminated groups on the exfoliated MXene nanosheets. Considering the merits of n-type CdS semiconductor, we further integrate 1D CdS nanorods with designed oxygen-terminated 2D MXene nanosheets. Our approach is to accelerate the electron-hole separation of semiconducting CdS and also to facilitate the charge transport at the interface by introducing highly conductive 2D MXene nanosheets with predominant oxygen-containing terminal groups. The presence of modified MXene in the heterojunction also leads to the extended utilization of wide-spectrum visible light. The unique feature of formed Schottky interface endows 1D CdS/2D MXene hybrid catalysts with high activity and long-term stability in hydrogen production from photocatalytic water splitting. Impressively, remarkable AQE enhancement was

DOI: 10.14102/j.cnki.0254-5861.2022-0151

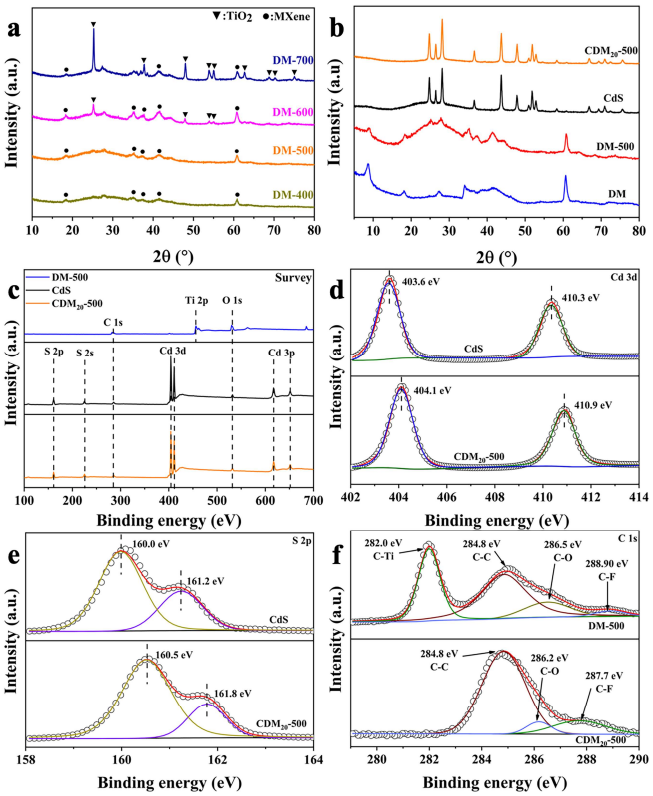

Figure 1. (a) Temperature-depended XRD patterns of DM (MXene nanosheets); (b) XRD patterns of DM, CdS, and CDM_{20}-500; (c) XPS survey spectra of CdS, MT-D500 and CdS/MT_{20}-D500 (CDM_{20}-500); (d, e) High-resolution XPS spectra of Cd 3d and S 2p in CdS and CDM_{20}-500; (f) High-resolution XPS spectra of C 1s in DM-500 and CDM_{20}-500.

observed at fixed monochromatic wavelengths (450 and 520 nm).

■ RESULTS AND DISCUSSION

MXene nanoflakes were prepared through intercalation and ultrasonication. Typically, DMSO solvent was used as the intercalator to enlarge the layer spacing of the bulk pristine MXenes (PM), and the delaminated MXenes (DM) were further obtained by ultrasonication. Subsequently, DM samples were annealed at different temperatures (T = 400, 500, 600, 700 °C) in argon atmosphere to obtain DM-X (X = 400, 500, 600, 700). The annealed MXenes were employed as the platform for the nucleation and in-situ growth of CdS nanorods by a solvothermal process. Varying the amount of Cd source obtained a series of CdS/MXene composites labeled as CDM_y-X (where y = 10, 20, 40, 80).

The structures and compositions of DM-X and CdS samples were analyzed by X-ray powder diffraction (XRD) and X-ray photoelectron spectroscopy (XPS). As shown in Figure 1a, when annealing above 600 °C, characteristic diffraction peaks (2θ = 25.3°, 37.8°, 48.0°, 53.9°, 55.1°, 62.7°, 68.8°, 70.3°, 75.0°) of TiO_2 were detected, indicating the formation of a large amount of TiO_2 at high temperature.[53,54] The XRD pattern of CdS shows a series of diffraction peaks at 24.8°, 26.5°, 28.2°, 36.6°, 43.7°, 47.8°, 51.8°, 58.3°, 66.8°, 70.9°, and 75.5° (Figure 1b), which can be assigned to (100), (002), (101), (102), (110), (103), (101), (202), (203), 8(211), and (105) lattice planes of hexagonal CdS. Unfortunately, no diffraction signal of MXene was detected in the composite CDM_{20}-500, which may be casued by weak diffraction signal and low dose of MXene. Figure 1c-d show the XPS spectra of CdS and CDM_{20}-500. The characteric peaks of Cd^{2+} $3d_{5/2}$ and Cd^{2+} $3d_{3/2}$ were probed in both CdS and CDM_{20}-500 (Figure 1d). Compared to CdS nanorods, CDM_{20}-500 showed higher binding energies of Cd^{2+} $3d_{5/2}$ and Cd^{2+} $3d_{3/2}$ (404.1 and 410.9 eV). Correspondingly, the binding energies of S^{2-} $2p_{3/2}$ and S^{2-} $2p_{1/2}$ shifted from 160.0 and 161.2 eV (CdS) to 160.5 and 161.8 eV (CDM_{20}-500) (Figure 1e), respectively. These phenomena reflect the decrease of surface electron density of CdS in CDM_{20}-500, indicating the strong interface interaction.[55] On the other hand, C 1s XPS spectrum of MXene was fitted into four peaks located at 282.0, 284.8, 286.5 and 288.9 eV (Fiugre 1f), which can be assigned to C-Ti, C-C, C-O and C-F bonds, respectively. Obviously, the binding energies of C-O and C-F shifted towards lower binding energies in CDM_{20}-500, suggesting an increase of surface electron density of MXene in CDM_{20}-500.[9,56]

SEM and TEM images of CDM_{20}-500 show that CdS nanorods are anchored on MXene nanosheets tightly (Figure 2a and 2c).[35] The TEM image of DM-500 (Figure 2b) shows a typical flake-like shape morphology and the lattice fringes with d-spacing of 1.0 nm. In the high-magnification TEM image of CDM_{20}-500 (Figure 2d), the lattice fringes belonging to MXene (d = 1.0 nm) and CdS (d = 0.37 nm) are observed in the forms of nanosheets and nanorods, respectively.[57] Furthermore, elemental mapping results of CDM_{20}-

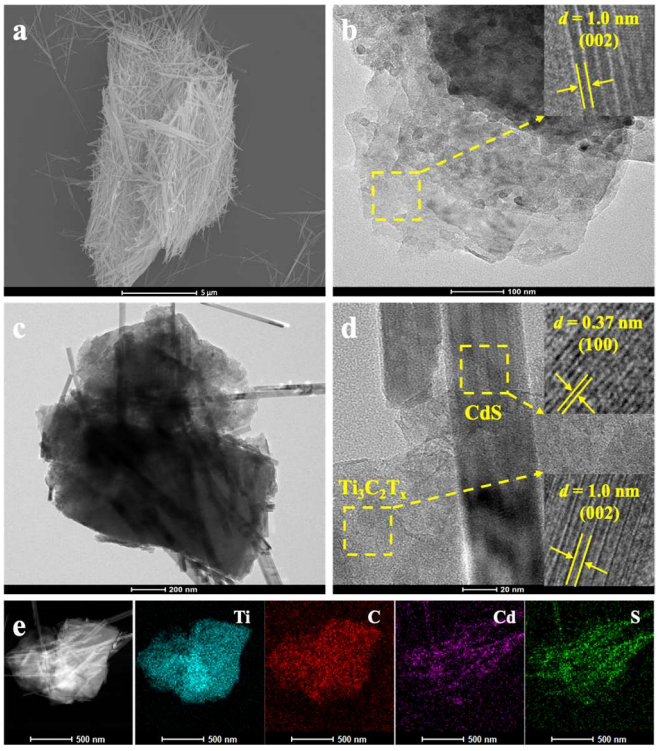

Figure 2. (a) SEM image of CDM_{20}-500, and TEM images of (b) annealed MXene (DM-500), (c, d) CDM20-500, and (e) the elemental mapping results of CDM20-500.

Chin. J. Struct. Chem. **2022**, 41, 2208058-2208064
DOI: 10.14102/j.cnki.0254-5861.2022-0151

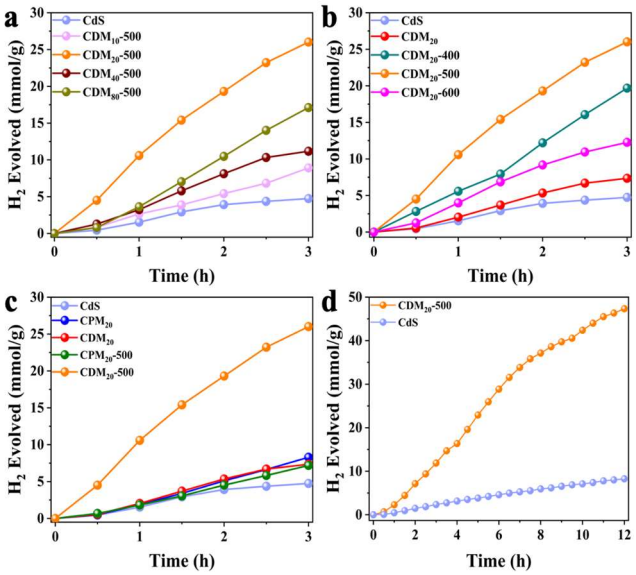

Figure 3. Photocatalytic H_2 evolution performance of CdS and CdS/MXene composites: (a) composites containing different dose of 500 °C annealed MXene; (b) composites containing the same dose of MXene annealed at different temperatures; (c) the performance comparison of the composites containing MXene and annealed MXene; (d) performance stability test of CdS and CDM_{20}-500.

500 show that Ti and C elements are distributed uniformly in the nanosheets, while Cd and S elements are clearly displayed in the nanorods (Figure 2e), confirming the successful construction of the heterojunction of CdS/MXene.[28]

In order to investigate the photocatalytic activity of CdS/MXene composites, photocatalytic hydrogen production rates of different composites were evaluated under visible light irradiation.[11] As shown in Figure 3a, CdS nanorods exhibit a low hydrogen evolution rate, while the composites CDM_y-500 (y = 10, 20, 40 and 80) show enhanced photocatalytic hydrogen production. Especially, CDM_{20}-500 displays the highest hydrogen production performance, which is about 5 times higher than that of CdS. To verify the optimum annealing temperature of MXene, the anneal process of DM was carried out at different temperatures (400, 500 and 600 °C) and fixed at a dosage of 20 mg before being used to construct composites (CDM-X, X = 400, 500, 600). The results of photocatalytic hydrogen evolution indicate that CDM_{20}-500 still possesses the highest hydrogen-evolving activity (Figure 3b). Moreover, the photocatalytic hydrogen evolution experiments over the nanocomposites hybridized with bulk MXene (PM) and intercalated MXene (DM) were conducted. As shown in Figure 3c, the nanohybrid of CDM_{20}-500 still illustrates the best hydrogen production performance. In addition, a long-term photocatalytic hydrogen evolution test on CDM_{20}-500 was carried out to evaluate its durability (Figure 3d). In the 12 h test, CDM_{20}-500 exhibits a steady increase in the evolved hydrogen under visible light illumination. AQE values of the optimized CDM_{20}-500 were calculated to be 35.6%, 27.8% and 18.1% at wavelengths of 420, 450 and 520 nm, respectively, which are higher than those reported in our previous work.[34]

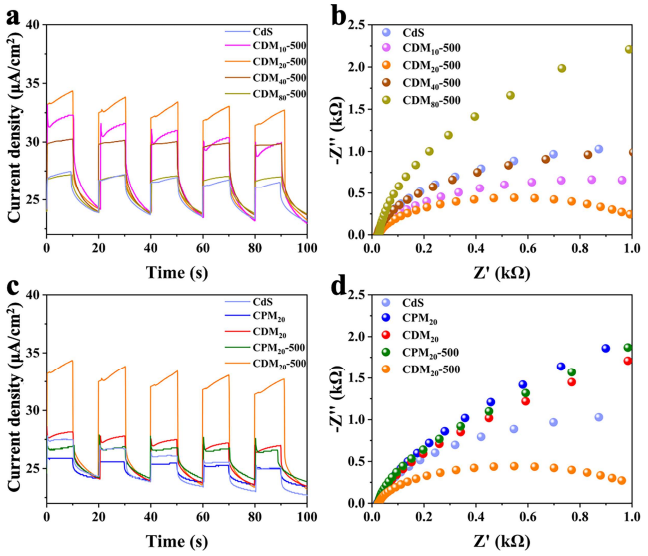

Figure 4. (a, c) Photocurrent density curves and (b, d) EIS Nyquist plots of CdS and CdS/MXene composites.

To explore the enhancement of photocatalytic hydrogen, the photocurrent response curves and EIS Nyquist plots were collected. With intermittent visible light, all the samples exhibited rapid and consistent response (Figure 4a, c), but only CDM_{20}-500 performed the highest response signal, indicating more photogenerated charge carriers forming in CDM_{20}-500. Correspondingly, CDM_{20}-500 showed the smallest semicircle of EIS Nyquist plots (Figure 4b, d), suggesting low resistance of charge migration. These results suggest that free photogenerated charges are more easily generated in CDM_{20}-500. This conclusion is further verified by in-situ electron spin resonance (ESR) results.[40] As shown in Figure 5a and 5b, the ESR signal attenuation of TEMPO (2,2,6,6-tetramethylpiperidine-1-oxyl, a typical electron and hole capturing

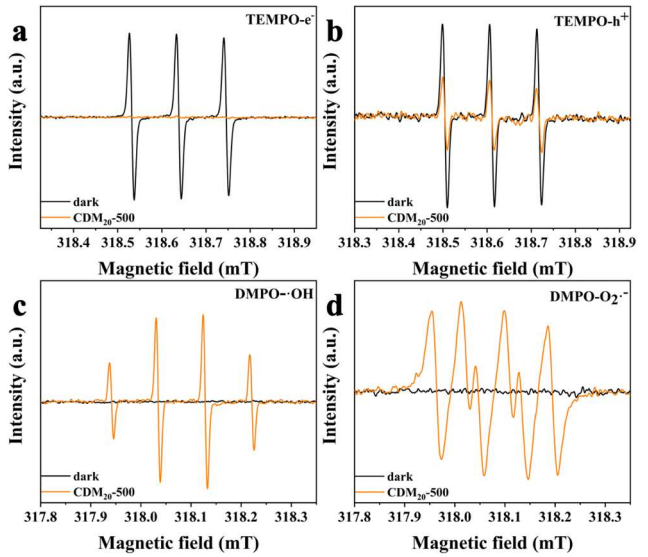

Figure 5. ESR spectra of radical adducts signal in dispersions of CdS and CdS/MXene composite: (a) electrons and (b) holes captured by TEMPO; (c) hydroxyl radical and (d) superoxide radical trapped by DMPO.

DOI: 10.14102/j.cnki.0254-5861.2022-0151

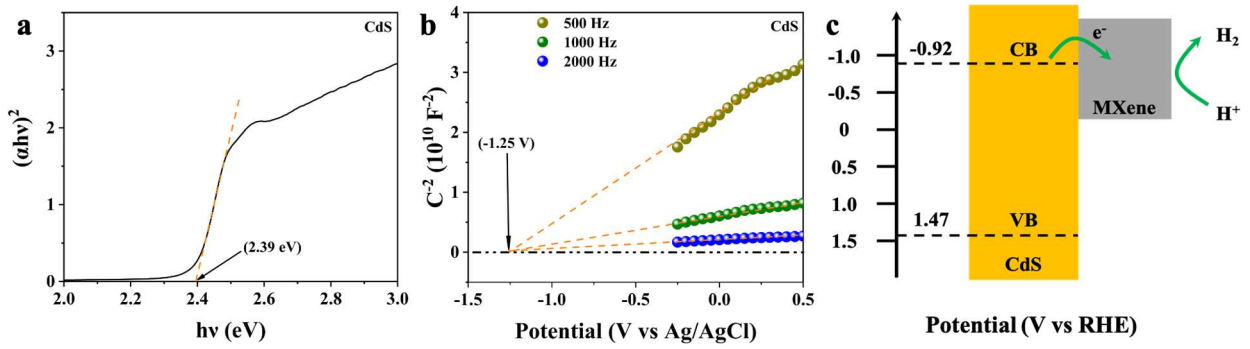

Figure 6. (a) $(\alpha hv)^2$ vs. hv plots and (b) the Mott-Schottky plots of CdS; (c) Representative schematic of CdS/MXene heterojunction for hydrogen production.

agent) is dramatic in CDM_{20}-500 dispersion under irradiation, indicating a large number of photogenerated electrons and holes on the surface of CDM_{20}-500.

To give insight into the redox capacity of photogenerated charge carriers, hydroxyl radical (·OH) and superoxide radical ($\cdot O_2^-$) were further detected by 5,5-dimethyl-1-pyrroline N-oxide (DMPO) due to the potentials of $O_2/\cdot O_2^-$ and $OH^-/\cdot OH$ which are -0.046 and 1.99 V vs. NHE, respectively.[58] Under visible light illumination, the ESR signals of DMPO-$\cdot O_2^-$ and DMPO-·OH adducts were significantly detected in CDM_{20}-500 dispersions (Figure 5c, 5d), indicating that the photogenerated electrons have sufficient proton reduction capacity.

The band position of CdS nanorods was determined. UV-vis DRS spectrum was converted into the $(\alpha hv)^2$ vs. hv plot through formula: $\alpha hv = A(hv - E_g)^{n/2}$, where n is determined by the type of a semiconductor (n = 1 for direct semiconductor and n = 4 for an indirect one), and α, h, v and A represent absorption coefficient, Planck's constant, vibration frequency and proportionality constant, respectively. The maximum slope tangent intersects the X-axis at 2.39 eV, indicating E_g = 2.39 eV. The conduction band (CB) of CdS nanorods was estimated according to the tangent of Mott-Schottky (M-S) curves (Figure 6b). Positive slopes at different frequencies suggest a typical n-type CdS, and the intercept on the X-axis determined the flat-band potentials (E_{fb}) to be -1.25 V (vs. Ag/AgCl), which was equivalent to -0.62 V (vs. RHE) according to the following formula[59]: $E_{RHE} = E_{Ag/AgCl} + 0.059\times pH + E^0_{Ag/AgCl}$ ($E^0_{Ag/AgCl}$ is about 0.199 V at 25 °C and pH is about 7.3). The value of CB can be calculated as -0.92 eV since its position is usually about -0.3 V above E_{fb}. Thus, the valence band (VB) can be calculated as 1.47 eV by the formula: $E_{VB} = E_{CB} + E_g$. Based on the above results, the band structure and electron migration of CDM_{20}-500 can be depicted in Figure 6c. The tight interface between MXene and CdS promoted the migration of photogenerated electrons from CdS to MXene, which is beneficial for the proton reduction.

■ CONCLUSION

In summary, we have successfully developed the approach to regulate the oxygen-terminated groups on the surface of $Ti_3C_2T_x$ MXene by a control thermal annealing process, constructing a novel heterojunction where 1D CdS nanorods are decorated on the modified 2D $Ti_3C_2T_x$ MXene nanosheets. The interfacial intimate contact between the annealed 2D MXene nanosheets and 1D CdS nanorods accelerates the separation and transport of photogenerated charge carriers. The optimized heterojunction photocatalyst CDM_{20}-500 containing 20 mg annealed MXene demonstrates improved hydrogen production performance, which is superior to those of pristine CdS and CdS/untreated MXene hybrid photocatalysts. AQE values of the optimal photocatalyst at 450 and 520 nm reach 27.8% and 18.1%, respectively.

■ EXPERIMENTAL

Synthesis and Surface Modification of $Ti_3C_2T_x$ MXene Sheets. Solvent intercalation is an effective way to delaminate MXene bulks (PM) into MXene sheets (DM).[40] Typically, 2 g MXene bulks was added into 50 mL DMSO, and stirred at room temperature in argon atmosphere for hours. The DMSO-intercalated MXene was collected by centrifugation and washed several times alternately with ethanol and deionized water. The intercalated MXene powder was then dispersed into deionized water through sonication dispersion method under continuous injection of argon. The layered Ti_3C_2Tx MXene sheets (DM) were centrifuged and dried in a vacuum at 60 °C for hours.

Five portions of the produced MXene sheets were annealed at 400, 500, 600 and 700 °C for 1 h, respectively at a heating rate of 5 °C/min in argon atmosphere. And the obtained samples are named DM-X (X = 400, 500, 600, 700). For comparison, MXene bulks were annealed at 500 °C for 1 h at the same heating rate in argon atmosphere, named PM-500.[48]

Synthesis of CdS/$Ti_3C_2T_x$ Composites. The sample DM-500 of different doses (10, 20, 40 and 80 mg) was dispersed into ethylenediamine by sonication treatment to prepare a homogeneous dispersion. The ethylenediamine solution of $Cd(NO_3)_2\cdot 4H_2O$ (20 mL) was dropped into the dispersion of exfoliated $Ti_3C_2T_x$ nanosheets, followed by stirring at room temperature for hours. The ethylenediamine solution containing thiourea was then slowly injected into the mixture and stirred for another 2 h. The final mixtures were transferred into Teflon-lined autoclaves, sealed and heated at 160 °C for 2 days. The obtained samples were washed several times alternately with ethanol and deionized water, and then dried under vacuum at 60 °C for 24 h, which were named CDM_y-500 (y = 20, 40, 80). The pure CdS nanorods were synthesized in the same strategy.

Characterization. The morphology and microstructure of sam-

Chin. J. Struct. Chem. **2022**, 41, 2208058-2208064
DOI: 10.14102/j.cnki.0254-5861.2022-0151

ples were observed by the field-emission scanning electron microscope (FESEM, FEI NovaNano SEM 450) and transmission electron microscope (TEM, FEI Tecnai G2 F30 S-TWIN) equipped with energy dispersive X-ray (EDX) analysis. X-ray photoelectron spectroscopy (XPS, Thermo Scientific ESCALAB 250 Xi) was used to determine the elemental composition of samples, and the obtained XPS spectra were referenced to the aliphatic C 1s peak of 284.8 eV. X-ray diffraction (XRD) patterns in the 2θ range of 5-80° were measured by an X-ray diffractometer equipped with Cu Kα radiation (Rigaku Ultima IV). UV-vis diffuse reflection spectroscopy (DRS) was performed on a UV spectrophotometer (UV2450) with $BaSO_4$ as reference in the range of 200-800 nm. Photoelectrochemical tests were performed on an electrochemical workstation (CHI 660E, Shanghai Chenhua) with a three-electrode system (Pt wire counter electrode, Ag/AgCl reference electrode and working electrode). Na_2SO_4 solution (0.1 M) was used as the electrolyte. Bruker A300-10/12 spectrometer was applied to detect the electron spin resonance (ESR) signals. The detection of photogenerated electrons and holes by TEMPO was performed severally in aqueous and acetonitrile solutions. The superoxide and hydroxyl radicals were detected in methanol and aqueous solutions respectively by using DMPO.

The photocatalytic water splitting experiments were carried out in a closed gas circulation-evacuation reactor (CEAULIGHT, CEL-SPH2N-D, 150 mL) which was connected to a water-cooling system. 10 mg of sample was added into a reactor containing 50 mL of lactic acid solution (10 wt.%). After ultrasonic dispersion, the reactor system was sealed and vacuumized. During photocatalytic reactions, the reaction system was continuously stirred and illuminated with a Xe lamp (PerkinElmer, 300 W, λ > 420 nm). Meanwhile, the cooling system kept the reactor temperature at 6 °C. To assess the rate of hydrogen release, the irradiation duration was set at 3 hours and measurements were taken at 30-minute intervals by a gas chromatography (GC-7920). The apparent quantum efficiency (AQE) at a fixed wavelength was calculated according to the following formula:[11]

$$\text{AQE}(\%) = \frac{2\times\text{number of evolved hydrogen molecules}}{\text{number of incident photons (N)}} \times 100\%$$

$$\text{N} = \frac{E\lambda}{hc}$$

Where E and λ are the intensity and wavelength of monochromatic light, respectively. The E values at 420, 450 and 520 nm are 267.2, 312.35, and 350.01 mW, respectively. h is the Planck constant (6.626×10^{-34} J·s) and c is the speed of light (3×10^8 m/s).

■ ACKNOWLEDGEMENTS

This work was supported by the National Natural Science Foundation of China (22005149, 21975129), Natural Science Foundation of Jiangsu Province (BK20200777), Natural Science Foundation of the Higher Education Institutions of Jiangsu Province, China (20KJB430034), Science Fund for Distinguished Young Scholars, Nanjing Forestry University (JC2019002), and Advanced Analysis and Testing Center, Nanjing Forestry University.

■ AUTHOR INFORMATION

Corresponding authors. Emails: xiaofei.yang@njfu.edu.cn (Prof. Xiaofei Yang) and chengxiaozhao@njfu.edu.cn (Dr. Chengxiao Zhao)

■ COMPETING INTERESTS

The authors declare no competing interests.

■ ADDITIONAL INFORMATION

Full paper can be accessed via
http://manu30.magtech.com.cn/jghx/EN/10.14102/j.cnki.0254-5861.2021-0151
For submission: https://mc03.manuscriptcentral.com/cjsc

■ REFERENCES

(1) Bai, X. J.; Hou, S. S.; Wang, X. Y.; Hao, D.; Sun, B. X.; Jia, T. Q.; Shi, R.; Ni, B. J. Mechanism of surface and interface engineering under diverse dimensional combinations: the construction of efficient nanostructured MXene-based photocatalysts. *Catal. Sci. Technol.* **2021**, 11, 5028-5049.
(2) Tang, M. L.; Ao, Y. H.; Wang, P. F.; Wang, C. All-solid-state Z-scheme WO_3 nanorod/$ZnIn_2S_4$ composite photocatalysts for the effective degradation of nitenpyram under visible light irradiation. *J. Hazard. Mater.* **2020**, 387, 121713.
(3) Li, K. Y.; Chen, J.; Ao, Y. H.; Wang, P. F. Preparation of a ternary g-C_3N_4-CdS/$Bi_4O_5I_2$ composite photocatalysts with two charge transfer pathways for efficient degradation of acetaminophen under visible light irradiation. *Sep. Purif. Technol.* **2021**, 259, 118177.
(4) Duan, C. X.; Yu, Y.; Xiao, J.; Li, Y. Y.; Yang, P. F.; Hu, F.; Xi, H. X. Recent advancements in metal-organic frameworks for green applications. *Green Energy Environ.* **2021**, 6, 33-49.
(5) He, B.; Feng, M.; Chen, X. Y.; Sun, J. Multidimensional (0D-3D) functional nanocarbon: promising material to strengthen the photocatalytic activity of graphitic carbon nitride. *Green Energy Environ.* **2021**, 6, 823-845.
(6) Yang, X. F.; Liu, W.; Han, C. H.; Zhao, C. X.; Tang, H.; Liu, Q. Q.; Xu, J. S. Mechanistic insights into charge carrier dynamics in $MoSe_2$/CdS heterojunctions for boosted photocatalytic hydrogen evolution. *Mater. Today Phys.* **2020**, 15, 110261.
(7) Lu, Y.; Cui, X. K.; Zhao, C. X.; Yang, X. F. Highly efficient tandem Z-scheme heterojunctions for visible light-based photocatalytic oxygen evolution reaction. *Water Sci. Eng.* **2020**, 13, 299-306.
(8) Yang, H.; Zhang, J. F.; Dai, K. Organic amine surface modified one-dimensional $CdSe_{0.8}S_{0.2}$-diethylenetriamine/two-dimensional $SnNb_2O_6$ S-scheme heterojunction with promoted visible-light-driven photocatalytic CO_2 reduction. *Chin. J. Catal.* **2022**, 43, 255-264.
(9) Di, T.; Cheng, B.; Ho, W.; Yu, J.; Tang, H. Hierarchically CdS-Ag_2S nanocomposites for efficient photocatalytic H_2 production. *Appl. Surf. Sci.* **2019**, 470, 196-204.
(10) Kuang, P.; Low, J.; Cheng, B.; Yu, J.; Fan, J. MXene-based photocatalysts. *J. Mater. Sci. & Tech.* **2020**, 56, 18-44.
(11) Ran, J.; Gao, G.; Li, F. T.; Ma, T. Y.; Du, A.; Qiao, S. Z. Ti_3C_2 MXene co-catalyst on metal sulfide photo-absorbers for enhanced visible-light photocatalytic hydrogen production. *Nat. Commun.* **2017**, 8, 13907.
(12) Tong, H.; Ouyang, S.; Bi, Y.; Umezawa, N.; Oshikiri, M.; Ye, J. Nano-photocatalytic materials: possibilities and challenges. *Adv. Mater.* **2012**, 24, 229-251.
(13) Chen, X.; Shen, S.; Guo, L.; Mao, S. S. Semiconductor-based photo-

catalytic hydrogen generation. *Chem. Rev.* **2010**, 110, 6503-6570.
(14) Kubacka, A.; Fernandez-Garcia, M.; Colon, G. Advanced nano-architectures for solar photocatalytic applications. *Chem. Rev.* **2012**, 112, 1555-1614.
(15) Zhang, J. F.; Fu, J. W.; Dai, K. Graphitic carbon nitride/antimonene van der waals heterostructure with enhanced photocatalytic CO_2 reduction activity. *J. Mater. Sci. Technol.* **2022**, 116, 192-198.
(16) Che, H. N.; Gao, X.; Chen, J.; Hou, J.; Ao, Y. H.; Wang, P. F. Iodide-induced fragmentation of polymerized hydrophilic carbon nitride for high-performance quasi-homogeneous photocatalytic H_2O_2 production. *Angew. Chem. Int. Edit.* **2021**, 60, 25546-25550.
(17) Li, J. H.; Ren, J.; Hao, Y. J.; Zhou, E. P.; Wang, Y.; Wang, X. J.; Su, R.; Liu, Y.; Qi, X. H.; Li, F. T. Construction of β-Bi_2O_3/$Bi_2O_2CO_3$ hetero-junction photocatalyst for deep understanding the importance of separation efficiency and valence band position. *J. Hazard. Mater.* **2021**, 401, 123262.
(18) Tang, M. L.; Ao, Y. H.; Wang, C.; Wang, P. F. Rationally constructing of a novel dual Z-scheme composite photocatalyst with significantly enhanced performance for neonicotinoid degradation under visible light irradiation. *Appl. Catal. B-Environ.* **2020**, 270, 118918.
(19) Guo, Y.; Ao, Y. H.; Wang, P. F.; Wang, C. Mediator-free direct dual-Z-scheme Bi_2S_3/$BiVO_4$/$MgIn_2S_4$ composite photocatalysts with enhanced visible-light-driven performance towards carbamazepine degradation. *Appl. Catal. B-Environ.* **2019**, 254, 479-490.
(20) Li, J. N.; Chen, J.; Ao, Y. H.; Gao, X.; Che, H. N.; Wang, P. F. Prominent dual Z-scheme mechanism on phase junction WO_3/CdS for enhanced visible-light-responsive photocatalytic performance on imidacloprid degradation. *Sep. Purif. Technol.* **2022**, 281, 119863.
(21) Mao, L.; Cai, X. Y.; Zhu, M. S. Hierarchically 1D CdS decorated on 2D perovskite-type $La_2Ti_2O_7$ nanosheet hybrids with enhanced photocatalytic performance. *Rare Metals* **2021**, 40, 1067-1076.
(22) Fan, Y. S.; Xi, X. L.; Liu, Y. S.; Nie, Z. R.; Zhao, L. Y.; Zhang, Q. H. Regulation of morphology and visible light-driven photocatalysis of WO_3 nanostructures by changing pH. *Rare Metals* **2021**, 40, 1738-1745.
(23) Zhao, Z. W.; Li, X. F.; Dai, K.; Zhang, J. F.; Dawson, G. In-situ fabrication of Bi_2S_3/$BiVO_4$/$Mn_{0.5}Cd_{0.5}S$-DETA ternary S-scheme heterostructure with effective interface charge separation and CO_2 reduction performance. *J. Mater. Sci. Technol.* **2022**, 117, 109-119.
(24) Huang, Y.; Mei, F. F.; Zhang, J. F.; Dai, K.; Dawson, G. Construction of 1D/2D $W_{18}O_{49}$/porous g-C_3N_4 S-scheme heterojunction with enhanced photocatalytic H_2 evolution. *Acta Phys.-Chim. Sin.* **2022**, 38, 2108028.
(25) Liu, Y.; Guo, J. G.; Wang, Y.; Hao, Y. J.; Liu, R. H.; Li, F. T. One-step synthesis of defected $Bi_2Al_4O_9$/β-Bi_2O_3 heterojunctions for photocatalytic reduction of CO_2 to CO. *Green Energy Environ.* **2021**, 6, 244-252.
(26) Cheng, L.; Xiang, Q.; Liao, Y.; Zhang, H. CdS-based photocatalysts. *Energy Environ. Sci.* **2018**, 11, 1362-1391.
(27) Ding, C.; Zhao, C.; Cheng, S.; Yang, X. Mixed-dimensional 1D CdS/2D $MoSe_2$ heterostructures for high-performance photocatalytic hydrogen production. *Surf. Interfaces* **2021**, 25, 101192.
(28) Wang, T.; Chai, Y.; Ma, D.; Chen, W.; Zheng, W.; Huang, S. Multi-dimensional CdS nanowire/$CdIn_2S_4$ nanosheet heterostructure for photocatalytic and photoelectrochemical applications. *J. Nano Res.* **2017**, 10, 2699-2711.
(29) Liu, X.; Sayed, M.; Bie, C.; Cheng, B.; Hu, B.; Yu, J.; Zhang, L. Hollow CdS-based photocatalysts. *J. Materiomics* **2021**, 7, 419-439.
(30) Tang, S.; Xia, Y.; Fan, J.; Cheng, B.; Yu, J.; Ho, W. Enhanced photocatalytic H_2 production performance of cds hollow spheres using C and Pt as bi-cocatalysts. *Chin. J. Catal.* **2021**, 42, 743-752.
(31) Feng, R.; Wan, K.; Sui, X.; Zhao, N.; Li, H.; Lei, W.; Yu, J.; Liu, X.; Shi, X.; Zhai, M.; Liu, G.; Wang, H.; Zheng, L.; Liu, M. Anchoring single Pt atoms and black phosphorene dual co-catalysts on CdS nanospheres to boost visible-light photocatalytic H_2 evolution. *Nano Today* **2021**, 37, 101080.
(32) Ding, M. Y.; Xiao, R.; Zhao, C. X.; Bukhvalov, D.; Chen, Z. P.; Xu, H. T.; Tang, H.; Xu, J. S.; Yang, X. F. Evidencing interfacial charge transfer in 2D CdS/2D MXene schottky heterojunctions toward high-efficiency photocatalytic hydrogen production. *Sol. RRL* **2021**, 5, 2000414.
(33) Li, Y. L.; Wang, X. J.; Hao, Y. J.; Zhao, J.; Liu, Y.; Mu, H. Y.; Li, F. T. Rational design of stratified material with spatially separated catalytic sites as an efficient overall water-splitting photocatalyst. *Chin. J. Catal.* **2021**, 42, 1040-1050.
(34) Xiao, R.; Zhao, C. X.; Zou, Z. Y.; Chen, Z. P.; Tian, L.; Xu, H. T.; Tang, H.; Liu, Q. Q.; Lin, Z. X.; Yang, X. F. In situ fabrication of 1D CdS nanorod/2D Ti_3C_2 MXene nanosheet schottky heterojunction toward enhanced photocatalytic hydrogen evolution. *Appl. Catal. B-Environ.* **2020**, 268, 118382.
(35) Alhabeb, M.; Maleski, K.; Anasori, B.; Lelyukh, P.; Clark, L.; Sin, S.; Gogotsi, Y. Guidelines for synthesis and processing of two-dimensional titanium carbide ($Ti_3C_2T_x$ MXene). *Chem. Mater.* **2017**, 29, 7633-7644.
(36) Zulfiqar, S.; Liu, S.; Rahman, N.; Tang, H.; Shah, S.; Yu, X. H.; Liu, Q. Q. Construction of S-scheme MnO_2@CdS heterojunction with core-shell structure as H_2-production photocatalyst. *Rare Metals* **2021**, 40, 2381-2391.
(37) Anasori, B.; Lukatskaya, M. R.; Gogotsi, Y. 2D metal carbides and nitrides (MXenes) for energy storage. *Nat. Rev. Mater.* **2017**, 2, 16098.
(38) Zhao, C. X.; Yang, X. F.; Han, C. H.; Xu, J. S. Sacrificial agent-free photocatalytic oxygen evolution from water splitting over Ag_3PO_4/MXene hybrids. *Sol. RRL* **2020**, 4, 1900434.
(39) Tan, Z. L.; Wei, J. X.; Liu, Y.; Zaman, F. U.; Rehman, W.; Hou, L. R.; Yuan, C. Z. V2CTx Mxene and its derivatives: synthesis and recent progress in electrochemical energy storage applications. *Rare Metals* **2022**, 41, 775-797.
(40) Lu, M.; Li, H.; Han, W.; Chen, J.; Shi, W.; Wang, J.; Meng, X.-M.; Qi, J.; Li, H.; Zhang, B.; Zhang, W.; Zheng, W. 2D titanium carbide (MXene) electrodes with lower-F surface for high performance lithium-ion batteries. *J. Energy Chem.* **2019**, 31, 148-153.
(41) Huang, X.; Wu, P. A facile, high-yield, and freeze-and-thaw-assisted approach to fabricate MXene with plentiful wrinkles and its application in on-chip micro-supercapacitors. *Adv. Funct. Mater.* **2020**, 30, 1910048.
(42) Amiri, A.; Chen, Y.; Bee Teng, C.; Naraghi, M. Porous nitrogen-doped MXene-based electrodes for capacitive deionization. *Energy Stor. Mater.* **2020**, 25, 731-739.
(43) Xi, Q.; Yue, X.; Feng, J.; Liu, J.; Zhang, X.; Zhang, C.; Wang, Y.; Wang, Y.; Lv, Z.; Li, R.; Fan, C. Facile synthesis of 2D $Bi_4O_5Br_2$/2D thin layer-Ti_3C_2 for improved visible-light photocatalytic hydrogen evolution. *J. Solid State. Chem.* **2020**, 289, 121470.
(44) Pang, S. Y.; Wong, Y. T.; Yuan, S.; Liu, Y.; Tsang, M. K.; Yang, Z.; Huang, H.; Wong, W. T.; Hao, J. Universal strategy for HF-free facile and rapid synthesis of two-dimensional MXenes as multifunctional energy materials. *J. Am. Chem. Soc.* **2019**, 141, 9610-9616.
(45) Kuang, P.; He, M.; Zhu, B.; Yu, J.; Fan, K.; Jaroniec, M. 0D/2D NiS_2/V-MXene composite for electrocatalytic H_2 evolution. *J. Catal.* **2019**, 375, 8-20.
(46) Oschinski, H.; Morales-García, Á.; Illas, F. Interaction of first row

DOI: 10.14102/j.cnki.0254-5861.2022-0151

transition metals with M_2C (M = Ti, Zr, Hf, V, Nb, Ta, Cr, Mo, and W) MXenes: a quest for single-atom catalysts. *J. Phys. Chem. C.* **2021**, 125, 2477-2484.
(47) Li, J.-Y.; Li, Y.-H.; Zhang, F.; Tang, Z.-R.; Xu, Y.-J. Visible-light-driven integrated organic synthesis and hydrogen evolution over 1D/2D CdS-$Ti_3C_2T_x$ MXene composites. *Appl. Catal. B-Environ.* **2020**, 269, 118783.
(48) Zhao, X.; Wang, Z.; Dong, J.; Huang, T.; Zhang, Q.; Zhang, L. Annealing modification of MXene films with mechanically strong structures and high electrochemical performance for supercapacitor applications. *J. Power Sources* **2020**, 470, 228356.
(49) Han, M.; Yin, X.; Wu, H.; Hou, Z.; Song, C.; Li, X.; Zhang, L.; Cheng, L. Ti_3C_2 MXenes with modified surface for high-performance electro-magnetic absorption and shielding in the X-band. *ACS Appl. Mater. Interfaces* **2016**, 8, 21011-21019.
(50) VahidMohammadi, A.; Rosen, J.; Gogotsi, Y. The world of two-dimensional carbides and nitrides (MXenes). *Science* **2021**, 372, 1581.
(51) Li, J.; Yuan, X.; Lin, C.; Yang, Y.; Xu, L.; Du, X.; Xie, J.; Lin, J.; Sun, J. Achieving high pseudocapacitance of 2D titanium carbide (MXene) by cation intercalation and surface modification. *Adv. Energy Mater.* **2017**, 7, 1602725.
(52) Zhang, Q.; Teng, J.; Zou, G.; Peng, Q.; Du, Q.; Jiao, T.; Xiang, J. Efficient phosphate sequestration for water purification by unique sandwich-like MXene/magnetic iron oxide nanocomposites. *Nanoscale* **2016**, 8, 7085-7093.
(53) Li, Z.; Wang, L.; Sun, D.; Zhang, Y.; Liu, B.; Hu, Q.; Zhou, A. Synthesis and thermal stability of two-dimensional carbide MXene Ti_3C_2. *Mater. Sci. Eng. C* **2015**, 191, 33-40.
(54) Feng, X. Y.; Wang, P. F.; Hou, J.; Qian, J.; Ao, Y. H.; Wang, C. Significantly enhanced visible light photocatalytic efficiency of phos-phorus doped TiO_2 with surface oxygen vacancies for ciprofloxacin degradation: synergistic effect and intermediates analysis. *J. Hazard. Mater.* **2018**, 351, 196-205.
(55) Feng, C.; Chen, Z.; Hou, J.; Li, J.; Li, X.; Xu, L.; Sun, M.; Zeng, R. Effectively enhanced photocatalytic hydrogen production performance of one-pot synthesized MoS_2 clusters/CdS nanorod heterojunction material under visible light. *Chem. Eng. J.* **2018**, 345, 404-413.
(56) Ding, M.; Xiao, R.; Zhao, C.; Bukhvalov, D.; Chen, Z.; Xu, H.; Tang, H.; Xu, J.; Yang, X. Evidencing interfacial charge transfer in 2D CdS/2D MXene schottky heterojunctions toward high-efficiency photocatalytic hydrogen production. *Sol. RRL* **2020**, 5, 2000414.
(57) Han, B.; Liu, S.; Zhang, N.; Xu, Y.-J.; Tang, Z.-R. One-dimensional CdS@MoS_2 core-shell nanowires for boosted photocatalytic hydrogen evolution under visible light. *Appl. Catal. B-Environ.* **2017**, 202, 298-304.
(58) Zhao, C.; Chen, Z.; Xu, J.; Liu, Q.; Xu, H.; Tang, H.; Li, G.; Jiang, Y.; Qu, F.; Lin, Z.; Yang, X. Probing supramolecular assembly and charge carrier dynamics toward enhanced photocatalytic hydrogen evolution in 2D graphitic carbon nitride nanosheets. *Appl. Catal. B-Environ.* **2019**, 256, 117867.
(59) Zhang, T.; Hou, Y.; Dzhagan, V.; Liao, Z. Q.; Chai, G. L.; Loffler, M.; Olianas, D.; Milani, A.; Xu, S. Q.; Tommasini, M.; Zahn, D. R. T.; Zheng, Z. K.; Zschech, E.; Jordan, R.; Feng, X. L. Copper-surface-mediated synthesis of acetylenic carbon-rich nanofibers for active metal-free photocathodes. *Nat. Commun.* **2018**, 9, 1140.

Received: June 9, 2022
Accepted: July 1, 2022
Published online: July 5, 2022
Published: July 25, 2022

DOI: 10.14102/j.cnki.0254-5861.2022-0151